Chemical Science

ROYAL SOCIETY OF CHEMISTRY

EDGE ARTICLE

View Article Online
View Journal | View Issue

Cite this: *Chem. Sci.*, 2021, **12**, 3751

All publication charges for this article have been paid for by the Royal Society of Chemistry

Design, scope and mechanism of highly active and selective chiral NHC–iridium catalysts for the intramolecular hydroamination of a variety of unactivated aminoalkenes†

Daven Foster,[a] Pengchao Gao,[a] Ziyun Zhang,[b] Gellért Sipos, ‡[a] Alexandre N. Sobolev,[c] Gareth Nealon,[c] Laura Falivene,§[b] Luigi Cavallo [b] and Reto Dorta *[a]

Received 26th October 2020
Accepted 4th January 2021

DOI: 10.1039/d0sc05884j

rsc.li/chemical-science

Chiral, cationic NHC–iridium complexes are introduced as catalysts for the intramolecular hydroamination reaction of unactivated aminoalkenes. The catalysts show high activity in the construction of a range of 5- and 6-membered N-heterocycles, which are accessed in excellent optical purity, with various functional groups being tolerated with this system. A major deactivation pathway is presented and eliminated by using alternative reaction conditions. A detailed experimental and computational study on the reaction mechanism is performed providing valuable insights into the mode of action of the catalytic system and pointing to future modifications to be made for this catalytic platform.

1. Introduction

Over the last decades, intense research has been devoted to developing catalytic alkene hydroamination (HA) protocols, as such a transformation would represent a very attractive route to valuable nitrogen-containing compounds starting from simple olefin and amine precursors.[1] An especially appealing factor of these classical HA reactions is the fact that they represent a rare example of a chemical transformation with almost perfect atom economy, with the only waste material generated being the spent catalyst.

While many studies have been devoted to advance the HA reaction with the ultimate goal of discovering catalytic systems able to couple the most simple HA partners, namely ammonia and ethylene, a possibly even more interesting application of the HA reaction lies in the area of asymmetric catalysis. Here, the same reaction is able to form chiral, amine-containing compounds that are ubiquitous scaffolds of natural products or synthetic drugs and are abundantly encountered in commodity and specialty chemicals. Among these, optically active N-heterocyclic compounds are of particular importance and are found in 59% of FDA approved drugs.[2] Six-membered rings, five-membered rings and fused rings are the most prevalent classes of ring systems. Specifically, both pyrrolidines and indolines are in the top five most common five-membered nonaromatic nitrogen heterocycles in FDA drugs (Fig. 1).[2] Piperidines, piperazines and morpholines all feature in the top 5 most common 6-membered N-heterocycles, with tetrahydroisoquinolines also being present in the structure of many natural products. Overall then, reactions targeting the formation and alteration of nitrogen heterocycles are of high interest and value.

Chiral N-heterocyclic compounds incorporating stereocenters adjacent to the nitrogen atom could potentially be accessed through the use of an enantioselective olefin HA reaction starting from the appropriate aminoolefin precursor molecules. Although great progress has been achieved over the

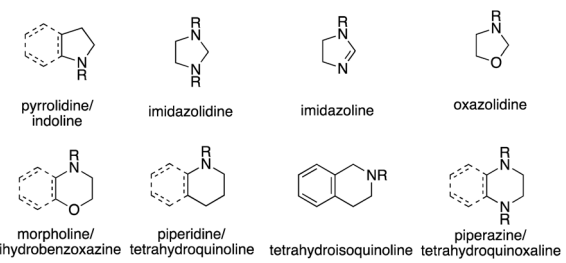

Fig. 1 Representative 5- and 6-membered N-heterocycles.

[a]*Department of Chemistry, School of Molecular Sciences, University of Western Australia, M310, 35 Stirling Highway, 6009 Perth, WA, Australia. E-mail: reto.dorta@uwa.edu.au*

[b]*King Abdullah University of Science and Technology (KAUST), Chemical and Life Sciences and Engineering, Kaust Catalysis Center, Thuwal 23955-6900, Saudi Arabia*

[c]*Centre for Microscopy, Characterisation and Analysis, University of Western Australia, 35 Stirling Highway, 6009 Perth, WA, Australia*

† Electronic supplementary information (ESI) available. CCDC 2022610. For ESI and crystallographic data in CIF or other electronic format see DOI: 10.1039/d0sc05884j

‡ Current address: ComInnex Inc., Zahony Utca 7, 1031 Budapest, Hungary.

§ Current address: Dipartimento di Chimica, Università di Salerno, Via Giovanni Paolo II, I-84084, Fisciano, Italy.

last two decades in developing such asymmetric HA reactions, they are still far from being well established. Furthermore, the variety of target structures has remained very limited and research has mostly focused on accessing methylated pyrrolidines in optically enriched form. Advances since Marks' and coworkers first reports of asymmetric intramolecular HA reactions (Fig. 2),[3] have concentrated on developing the original rare-earth systems and have expanded to include alkali and alkaline earth metal catalysts as well as early-transition metal compounds.[4] Indeed, results by the groups of Schafer,[5] and most recently Sadow,[6] have shown that chiral zirconium catalysts are able to provide pyrrolidine products with high enantiopurity and represent the current state of the art for these asymmetric transformations. The major drawback that remains with these catalytic systems is their highly sensitive nature and very limited functional group tolerance that impedes a broader implementation of this elegant synthetic methodology within the chemical community. Moreover and as discussed above, these systems have not been applied successfully to substrate classes other than pyrrolidines, *e.g.* to indolines, piperidines or similar.

Substitution of these air and moisture sensitive compounds with more tolerant late-transition metal (LTM) catalysts would without a doubt alleviate the problem, but the asymmetric HA reaction of electronically unbiased amines and simple olefins has not yet been developed to the same degree with these metals. For example, a single report exists in the literature for the asymmetric intramolecular HA to access pyrrolidines, in which Buchwald *et al.* use a cationic rhodium system with chiral MOP-type ligands.[7] In terms of developing intermolecular versions of the asymmetric hydroamination reaction with LTMs, known examples that employ simple olefins and amines are normally restricted to very particular types of olefins and amines as exemplified in Fig. 3.[8,9] Progress has been made in this field over the last few years through discoveries pioneered by Miura and Buchwald,[10,11] who were able to overcome some of these limitations by introducing formal intermolecular HA reactions that use electrophilic aminating reagents and rely on the use of an exogenous hydrogen source. These advances though come at a price, as these processes employ super-stoichiometric amounts of additives and are thus moving away from the concept of atom economy epitomized by the classical

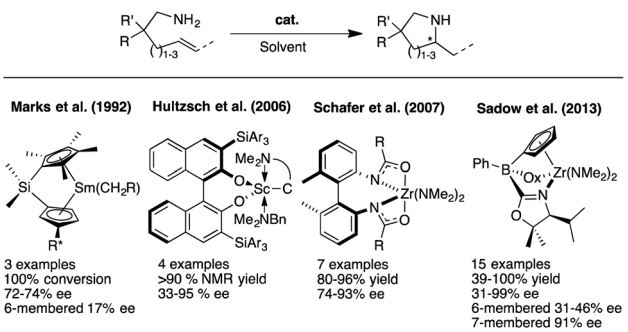

Fig. 2 Asymmetric intramolecular HA reaction with lanthanides and early-transition metals based catalysts.

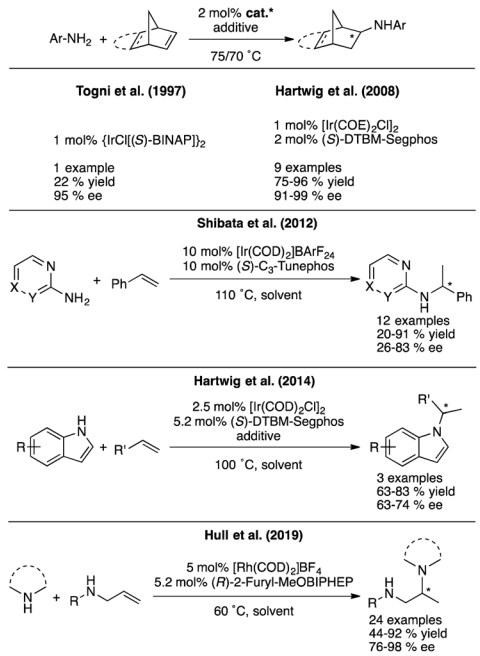

Fig. 3 Asymmetric intermolecular HA with simple amines/olefins.

HA reaction. Furthermore, because these reactions are catalyzed by Cu–H species, they again pose unfortunate limitations in terms of functional groups being tolerated (*i.e.* reducible functional groups such as carbonyl groups).

Our entry into the asymmetric HA reaction was inspired by a report where Stradiotto *et al.* had shown that simple $[IrCl(COD)]_2$ can act as a precatalyst in the intramolecular HA reaction (Fig. 4, top left).[12] Attempts by the same group at developing chiral versions failed.[13] Because one of our main research themes evaluates the use of chiral sulfoxides as ligand entities in asymmetric metal catalysis,[14] we began studying Ir-disulfoxides of general formula $[Ir(disulfoxide)Cl]_2$ for the

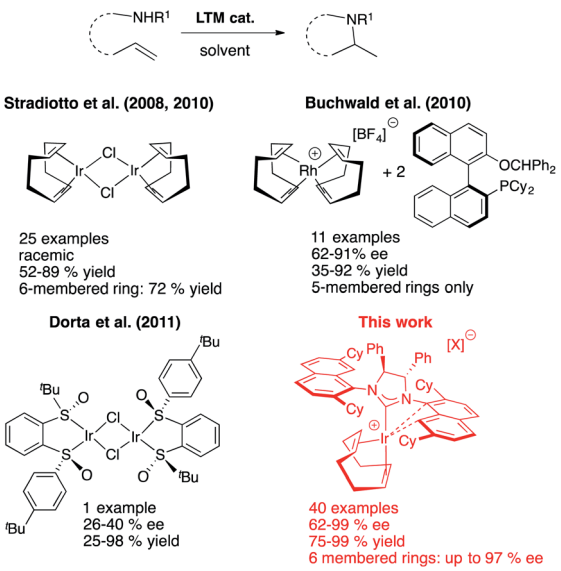

Fig. 4 Selected LTM systems for the intramolecular HA reaction.

asymmetric intramolecular HA (Fig. 4, bottom left).[15] While these initial trials reached appreciable reactivity when applied to the generic intramolecular HA reaction of *N*-benzyl-2,2-diphenylpent-4-en-1-amine, they also showed rather low enantioselectivity (a maximum of 40% ee).

In the last few years, our group surmised that a potentially more successful approach for increasing reactivity (and with it the enantioselectivity) would be to use harder, cationic and monomeric $[(L)_3Ir]^+$ systems. To keep the overall electronic situation in these complexes similar to the neutral, catalytically active IrCl(COD) fragment developed by Stradiotto, we speculated that substitution of the anionic halide with an electron-rich, chiral N-heterocyclic carbene (NHC) ligand might provide a direct entry to catalytically active, monomeric complexes of formula $[Ir(NHC^*)(COD)]^+$. Given the high propensity of iridium compounds to undergo cyclometallation events, we were well aware of the fact that such formally 14-electron complexes might not be isolable, especially in light of literature precedents with classical aryl-substituted NHCs that undergo such decomposition events.[16]

Gratifyingly though, first attempts indicated that the special naphthyl-substituted side chain groups that characterize our family of NHCs,[17] is able to prevent decomposition of these $[Ir(NHC)(COD)]^+$ compounds by creating a stabilizing interaction between the empty coordination site on the metal and one of these naphthyl side chains.[18] Even more rewarding was the fact that this first system showed markedly enhanced reactivity compared to the simple system developed by Stradiotto and allowed us to access optically highly enriched pyrrolidines when introducing enantiopure $[Ir(NHC^*)(COD)]^+$ catalysts.[19]

Herein, we provide a complete account of our studies using $[Ir(NHC^*)(COD)]^+$ catalysts for the asymmetric intramolecular hydroamination (HA). The first aim of the study was to understand whether incorporation of a more electron-rich backbone onto our chiral NHC ligand would generate a more active catalyst while maintaining the high selectivity seen in our preliminary report with (R_a,R_a,*S*,*S*)-[(DiPh-2,7-SICyNap)Ir(COD)][X]. This was realized by substituting the chiral diphenyl backbone with a chiral, fused cyclohexyl unit, an approach that has so far not been successful in chiral NHC ligand design.[20] Secondly, we sought to expand the substrate scope of the asymmetric intramolecular hydroamination of unactivated aminoolefins, focusing in particular on testing substrates that contain functional groups that clearly sets this system apart from known catalysts and on ring systems that have not been investigated previously. Furthermore and most relevant to future developments of this catalyst platform, we present a detailed mechanistic investigation that employs a combination of experimental and computational techniques revealing the likely processes at play for the enantioselective formation of the products.

2. Results and discussion

2.1 Cationic [(NHC*)Ir(COD)][X] precatalysts

Optically pure (*S*,*S*)-diphenyldiamine or (*R*,*R*)-diaminocyclohexane were incorporated into the backbone of the NHC ligand using two identical 2,7-dicyclohexyl-1-naphthyl units as side chains, giving NHC salts (DiPh-2,7-SICyNap·HBF_4) (**1**) and neutral iridium complex [(R_a,R_a,*S*,*S*)]-**2**Cl, as well as (2,7-FuCySICyNap·HBF_4) (**3**) and diastereomers of complex **4**Cl. Ultimately, this led to the synthesis of six cationic iridium complexes whose structure is shown in Fig. 5.

While synthetic details, a discussion as well as full characterization can be found in the ESI,†[21] we may point out the fact that these cationic, formally 14-electron complexes all show fluxional behavior. The apparent fluxionality that we see in solution on the ^{1}H NMR time scale may originate from either a windshield-wiper mechanism as depicted on the top of Fig. 6 or from rotation around the NHC–[Ir] axis in a helicopter-type movement (bottom of Fig. 6), with the latter being more likely.[22]

2.2 Comparison of catalyst performance

We started our catalytic investigation by taking complexes **2**[X] and **4**[PF_6] and applying them to the model substrate *N*-benzyl-2,2-diphenylpent-4-en-1 amine (**5a**) to access the corresponding methylated pyrrolidine product **5b**. Reactions were conducted in NMR tubes using CD_2Cl_2 in order to be able to follow conversions in real time, at relatively high concentrations (0.6 M, 0.5 mL solvent volume), and fixing the catalyst loadings at 2 mol%. This first set of experiments (Fig. 7) was performed using the four catalysts with the identical PF_6^- counteranion. [(R_a,R_a,*R*,*R*)]-**4**[PF_6] (in red) outperformed [(R_a,R_a,*S*,*S*)]-**2**[PF_6] (in blue) and especially its diastereomeric sibling [(R_a,S_a,*R*,*R*)]-**4**[PF_6] (grey) and [(S_a,S_a,*R*,*R*)]-**4**[PF_6] (green). Indeed, this latter catalyst was not able to fully convert the substrate.

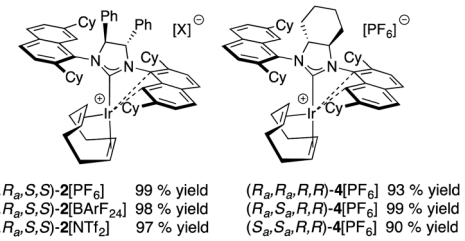

Fig. 5 Chiral cationic NHC–iridium complexes for catalytic testing.

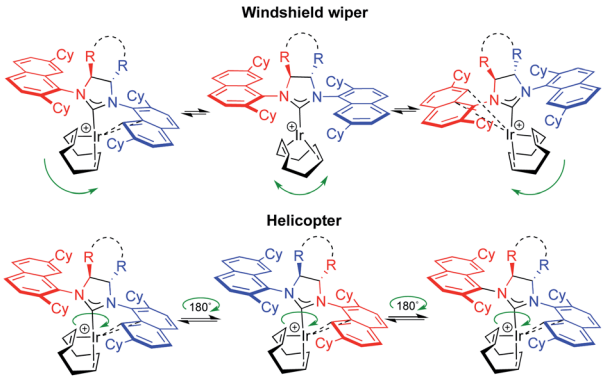

Fig. 6 Possible ligand movements explaining fluxionality in **2**[X]. Top: COD flip. Bottom: rotation around the NHC–Ir bond.

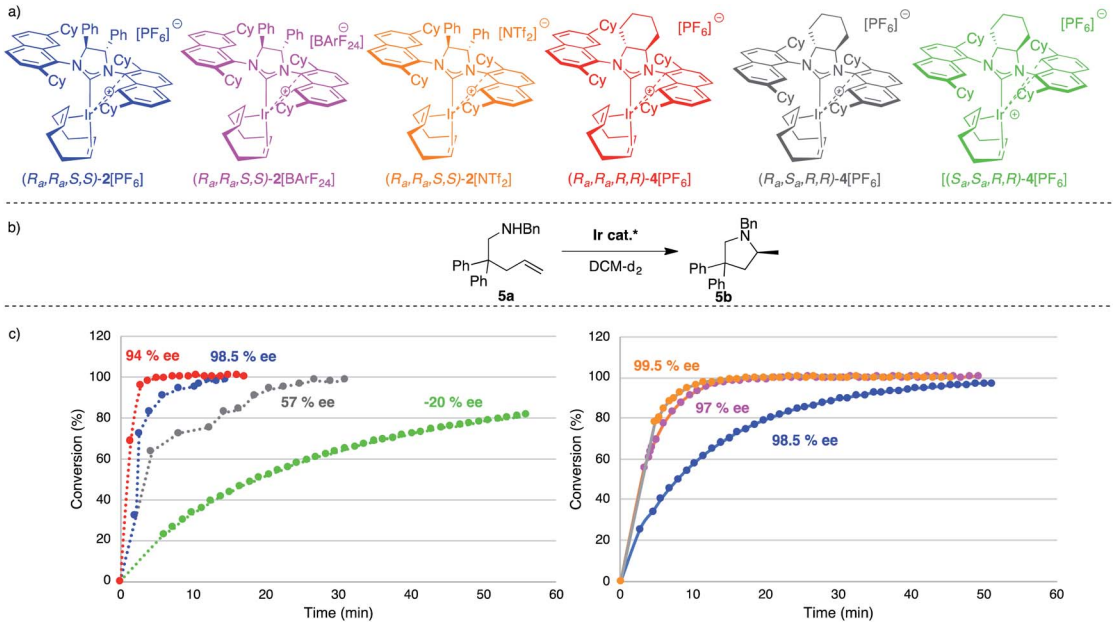

Fig. 7 (a) Catalyst structures tested in the intramolecular HA reaction of **5a**. (b) Catalytic HA reaction of model substrate **5a**. (c) Plot of conversion (%) of substrate **5a** to pyrrolidine **5b** *vs.* time (min) (left) for four different NHC*–[Ir] complexes at 2 mol%. DCM-d_2 (0.5 mL), [**5a**] = 0.6 M, [Ir] = 0.012 M. Plot of conversion (%) of substrate **5a** to pyrrolidine **5b** *vs.* time (min) (right) for (R_a,R_a,*S*,*S*)-**2**[X] at 1 mol% where X is PF_6, $BArF_{24}$ or NTf_2. DCM-d_2 (0.5 mL), [**5a**] = 0.6 M, [Ir] = 0.006 M. Monitored using ^{1}H NMR.

Enantioselectivity though followed the opposite trend for the two top-performing catalysts, where [(R_a,R_a,*S*,*S*)]-**2**[PF_6] was more selective (98.5% ee) than [(R_a,R_a,*R*,*R*)]-**4**[PF_6] (94% ee). Here again, [(R_a,S_a,*R*,*R*)]-**4**[PF_6] and [(S_a,S_a,*R*,*R*)]-**4**[PF_6] were not competitive and showed vastly diminished (and reversed) selectivity (57% ee and −20% ee respectively). In this context, two comments are warranted here. First, the enantioselectivity for **5b** recorded with [(R_a,R_a,*S*,*S*)]-**2**[PF_6] sets a new benchmark for systems that use substrate **5a** (or its primary amine analogue) and underline the validity of the catalyst design. Second, [(R_a,R_a,*R*,*R*)]-**4**[PF_6] is the first catalyst to feature a fused cyclohexyl backbone in its NHC ligand design which shows high levels of enantiodiscrimination.[20]

Overall though, we selected catalyst [(R_a,R_a,*S*,*S*)]-**2**[PF_6] based on its combination of high activity and excellent selectivity. Before moving to test its applicability to a diverse range of substrates, we nevertheless decided to perform a small study on the effect of the gegenion on the reaction outcome (Fig. 7). For this, we introduced $BArF_{24}^-$ as a well-known and successful alternative to PF_6^- in iridium catalysis,[23] and also tested the NTf_2^- counteranion, a moiety that to the best of our knowledge has never been investigated in iridium (or rhodium) chemistry.[24] The outcome of this study, where the catalyst loading was lowered to 1 mol%, was rather unexpected as it showed that **2**[NTf_2] outperformed not only **2**[PF_6], but was also slightly more active than **2**[$BArF_{24}$]. Overall reaction rates are impressively high with corresponding TOF_{50} values increasing from 377 h^{-1} (for **2**[PF_6]), to 1071 h^{-1} (for (**2**[$BArF_{24}$]), all the way to 1500 h^{-1} for **2**[NTf_2], placing these catalysts on par or above the most active HA catalysts reported (rare-earth systems). Analysing the optical purity of product **5b** also produced rather unexpected data, as enantiomeric ratios of **5b** varied from *ca.* 66 : 1 er (with **2**[$BArF_{24}$]) to *ca.* 200 : 1 er (with **2**[NTf_2]).

2.3 Catalytic results for pyrrolidine-type products

With these results in hand, we moved ahead and started a broader investigation into the substrate scope to access optically enriched, methylated pyrrolidine products using **2**[NTf_2] as the catalyst of choice and the results are tabulated below (Table 1). In the first row of reported products (**5b–12b**), we systematically varied the nitrogen substituent of the starting material. This was done in order to gain insights into functional group tolerance and also because the only other LTM system reported thus far is extremely sensitive to slight changes of this benzyl group.[7a] With catalyst **2**[NTf_2], products **5b** to **12b** are uniformly accessed in high yield and with excellent optical purity, in some cases approaching complete selectivity. Functional group tolerance was just as satisfying, with the different benzyl substitutions leading to excellent reaction outcomes. When analyzing possible electronic effects of these substitutions by looking at the k_{obs} or TOF_{50} value, we do not see any apparent trend that relates reactivity to the electronic nature of the benzyl substitution. Replacing these benzyl groups with purely aliphatic substituents is equally successful (**11b**, **12b**), although a slight erosion in enantioselectivity can be seen for the methyl substituted substrate **12a** (incidentally, **12a** also shows the fastest reaction rate). This probably indicates that a more sterically encumbered *N*-substituent (**5a** to **11a**) is beneficial for selectivity and is recognized by the catalyst structure. When switching to the similarly sized, but electronically distinct *N*-phenyl substituent, reactivity decreased dramatically and the

Table 1 Cyclization of aminoalkenes to pyrrolidines using catalyst **2**[NTf_2][a]

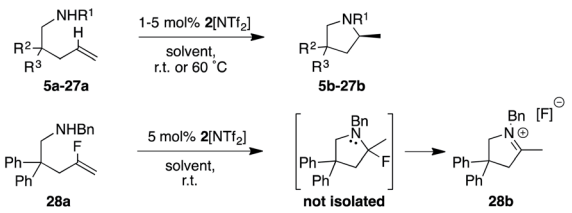

Product	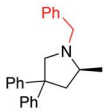	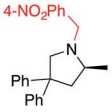	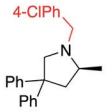	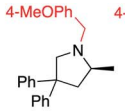	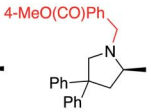	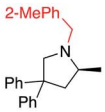	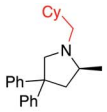	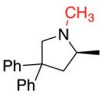
	5b	**6b**	**7b**	**8b**	**9b**	**10b**	**11b**	**12b**
ee (%)	>99	98	97	98	>99	>99	99	90
Yield[b] (%)	95	92	91	95	89	91	92	89
k_{obs} (10^{-2} min^{-1})	31[c]	20	92	49	54	25	9.4	>71[d]
TOF_{50} (h^{-1})	1357[c]	437	1969	1312	1148	520	211	>1500[d]

Product	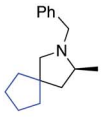	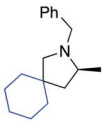	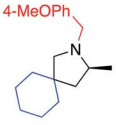	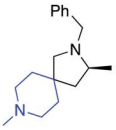	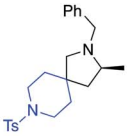	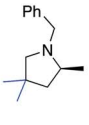		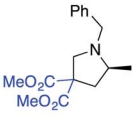
	13b	**14b**	**15b**	**16b**	**17b**	**18b**	**19b**	**20b**
ee (%)	97	99	96	98	>99	98	96	>99[e]
Yield (%)	96	93	96	81	95	95	88	75
k_{obs} (10^{-2} min^{-1})	2.3	17	1.7	>52[d]	12	1.9	1.5	41
TOF_{50} (h^{-1})	49.4	265	37.5	>1125[d]	258	42.0	32.6	1312

Product	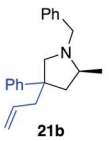	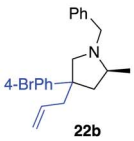	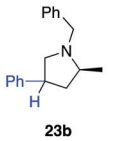	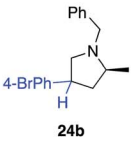	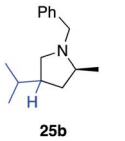	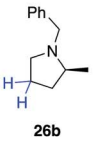	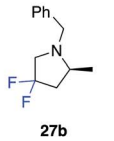	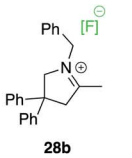
	21b	**22b**	**23b**	**24b**	**25b**	**26b**	**27b**	**28b**
ee (%)	97/99[f,g]	99/99[f,g]	94/77[f,g]	96/76[f,g]	86/63[f,g]	20[f,h]	88[e,f] (87)[f,i]	n/a
Yield (%)	93	92	90	93	94	69	85 (93)	91[e,f]
k_{obs} (10^{-2} min^{-1})	68	75	18	7	3.4	—	—	0.73[j]
TOF_{50} (h^{-1})	1467	1479	156	62.8	74.4	—	—	6.4[j]

[a] Conditions: [substrate] = 0.6 M, 2 mol% Ir cat., solvent = CD_2Cl_2 unless otherwise stated. Yields and ee values reported as an average of duplicate runs. [b] Isolated yield. [c] 1 mol% Ir. [d] k_{obs} and TOF_{50} values extrapolated from data as reaction finished upon first ^1H NMR scan (see ESI for details). [e] r.t. in TFT. [f] 5 mol% Ir. [g] Diastereomeric ratios: 1.1 : 1 (**21b**, **22b**), 3 : 4 (**23b**), 1 : 1 (**24b**), 3 : 2 (**25b**). Isolated yields are for the mixture of diastereomers. [h] 80 °C in 1,2-$C_6H_4F_2$. [i] 60 °C in ^{t}BuOH. [j] Product precipitates out of solution in NMR tube, so observed k_{obs} and TOF_{50} are only a (conservative) estimate.

corresponding product is no longer obtained in optically enriched form (92% yield, 9% ee, see ESI†).[25]

Various 3,3′-substituted spirocyclic pyrrolidine products **13b–17b** were accessed next as shown in the second row of Table 1. Here again, excellent reactivity produced methylated pyrrolidines with very high optical purity. Hydrocarbon-based spirocycles **13a–15a** as well as dimethyl-substituted substrates **18a** and **19a** provided high yields and enantioselectivities of the products. A spirocyclic, *N*-tosyl protected piperidine substrate (**17a**) was perfectly amenable to undergo cyclization, highlighting the functional group tolerance of the present LTM system. Substrate **20a** featuring an electron-poor, malonate-derived 2,2′-substituted backbone again gave essentially optically pure product **20b**. While conversion to product was quantitative, subsequent purification steps resulted in slightly lower isolated yields. The yield of **16b** with an *N*-methyl substituted piperidine spirocycle suffered from what appears to be catalyst inhibition and/or rapid catalyst decomposition as observed in the corresponding time/conversion graph (see ESI†).

The next class of compounds tested featured unsymmetrically 2,2′-disubstituted substrates (**21a–25a**). All of these compounds underwent cyclization to give diastereomer mixtures. Within this category, 2,2′-disubstituted **21a** and **22a**

gave rise to two diastereomers in roughly equal amount, with both resulting products showing excellent optical purity. Kinetic resolution was also not observed in the case of racemic *N*-benzyl-2-phenylpent-4-en-1-amine, *N*-benzyl-2-(4-bromophenyl)pent-4-en-1-amine or *N*-benzyl-2-isopropylpent-4-en-1-amine (**23a–25a**), again giving rise to diastereomer mixtures in approximately equal amounts. Not surprisingly, the single backbone substitution in the substrates resulted in lower overall reactivity, but reactions could still be run at room temperature giving high yields of isolated product. The enantioselectivity of one of the diastereomers was consistently higher than that of the other. A straightforward explanation for these results would see a scenario where the backbone substrate substitution is recognized by the catalyst structure, and where omitting it (H instead of R) would lead to a certain loss of enantioselection due to a less ordered transition state (see also 2.9 for *in silico* discussions).

Gratifyingly, a 2,2′-difluoro substituted aminoalkene (**27a**) was also amenable to cyclization to give the corresponding fluorinated pyrrolidine product in high yield and optical purity (93% yield, 88% ee). Such partially fluorinated pyrrolidines are of central importance in drug development,[26] and our results show how the asymmetric HA reaction might be used for accessing this family of compounds. Unfortunately, replacing the fluorine atoms by hydrogens and trying to ring-close the parent *N*-benzyl-pent-4-en-1-amine (**26a**) was not successful. While the intramolecular HA reaction did occur under forcing conditions (80 °C, 5 mol% cat.) to give acceptable yields of **26b** (69%), the enantioselectivity of the transformation was negligible (20% ee). The last entry of Table 1 shows the unexpected outcome when subjecting *N*-benzyl-4-fluoro-2,2-diphenylpent-4-en-1-amine (**28a**) to the intramolecular HA reaction. This substrate was chosen as a representative to possibly access a chiral quaternary carbon atom featuring a C–F bond. While the ring-closing itself proceeded unexpectedly smoothly and rapidly, we were not able to isolate the desired product as it rapidly formed iminium fluoride **28b** in close to quantitative yield. Whereas the outcome was unfortunate, it should be pointed out that product **28b** represents what appears to be the first example of a naked fluoride containing the 3,4-dihydro-2*H*-pyrrolium cation motif.[27]

2.4 Catalyst decomposition and further optimisation

2.4.1 Menshutkin reaction/product contamination. For some of the more challenging reaction runs shown in Table 2 (*e.g.* single backbone substitution in the starting material, **23a–25a**), NMR analysis of the mixture at the end of the catalytic run revealed that a substantial part of the catalyst had transformed back to the neutral, catalytically inactive (R_a,R_a,*S*,*S*)-**2**Cl precursor as evidenced by the appearance of diagnostic signals in their ^{1}H and ^{13}C NMR spectra. Specifically and taking the transformation of **24a** to **24b** as an example, the upfield protons involved in the C–H/π interaction between the backbone phenyl and the 2-cyclohexyl group of the NHC ligand split into two signals at *ca.* −0.16 and −0.54 ppm, the H_8 proton of the naphthyl side chain experiences a downfield shift to *ca.* 8.79 ppm, and most diagnostically, the carbene signal appears at *ca.* 209 ppm (see ESI† for details).[28] There is no evidence for (R_a,R_a,*S*,*S*)-**2**[NTf_2] in the spectrum (carbene peak *ca.* 188 ppm).[29] Formation of (R_a,R_a,*S*,*S*)-**2**Cl must involve the DCM solvent as the only plausible source of chloride.

Unfortunately, a literature search on relevant decomposition of cationic [Ir]$^+$ species, used extensively as catalysts to promote (asymmetric) hydrogenation reactions in DCM, did not yield any pertinent information. (R_a,R_a,*S*,*S*)-**2**Cl seems to be produced from the reaction of the pyrrolidine product **24b** (a tertiary amine) with the methylene chloride solvent through a nucleophilic substitution reaction (Menshutkin reaction). Generally, these types of reactions are very slow with a half-life for trimethylamine and CH_2Cl_2 of a month,[30] although well-defined and confined macrocycles are known to greatly accelerate the reaction.[31] In our case, it is reasonable to assume that the highly electrophilic nature of our catalyst is able to intermittently bind DCM and thus significantly activate the carbon atom towards nucleophilic attack of our pyrolidine product as shown in Fig. 8 (bottom center).[32] The resulting, partially deuterated ammonium salt **24c** was indeed identified *via* high-resolution mass spectrometry after the catalytic reaction run.

The generation of neutral chloro-complex (R_a,R_a,*S*,*S*)-**2**Cl during catalysis unfortunately also leads to product contamination as **2**Cl cannot be separated and removed efficiently during workup and column chromatographic purification of the organic products. Such behavior has been problematic in other catalytic transformations, most notably with spent ruthenium-catalysts used in metathesis reactions.[33] After unsuccessfully applying a literature procedure for removal of Grubbs-type ruthenium catalyst contaminants,[32a] we developed a protocol where the cationic iridium complex is reformed as its **2**[PF_6] salt. The salt can then be separated after the reaction run by extracting the organic product into a nonpolar solvent at the beginning of the chromatographic purification procedure (see the ESI† for details). Nevertheless and before moving forward and expanding the substrate scope for catalyst **2**[NTf_2], we wanted to identify a more suitable solvent where decomposition of the catalyst as described here can be excluded.

2.4.2 Alternative reaction solvents. Initially, ^{t}BuOH was chosen as a potential substitute for DCM. While we were delighted to see that a protic solvent such as ^{t}BuOH represents a suitable reaction medium (a run with model substrate **5a** giving high yield and similar enantioselectivity to DCM), solubility issues arose which prevented reactions to be performed at room temperature. We then identified trifluorotoluene (TFT) as another potential alternative, as it has been used as a DCM substitute in both organic reactions and more recently in metal-catalyzed transformations.[34] Besides having the added benefit of a higher boiling point than DCM, applying a simple presaturation solvent suppression sequence also made it amenable to monitoring catalytic conversions *via* ^{1}H NMR spectroscopy. To understand and compare the solvents' behavior under catalytic conditions, we first monitored the conversion of model pyrrolidine precursor **5a** at 1 mol% **2**[NTf_2] (see ESI†), resulting in similar reaction speeds for DCM-d_2 ($k_{obs} = 27.0 \times 10^{-2}$) and TFT ($k_{obs} = 34.2 \times 10^{-2}$).

Gratifyingly, the superior performance of TFT became apparent under more challenging reaction conditions (0.5 mol% **2**[NTf_2]). At this very low loading where catalyst decomposition is becoming problematic, full conversion of **5a** is no longer observed in DCM-d_2 (*ca.* 70% maximum conversion, k_{obs} value of 3.1×10^{-2}, Fig. 9). On the other hand, when the same reaction is performed in TFT at room temperature, full conversion of **5a** to **5b** was observed together with a substantial increase in reaction rate ($k_{obs} = 14.3 \times 10^{-2}$).

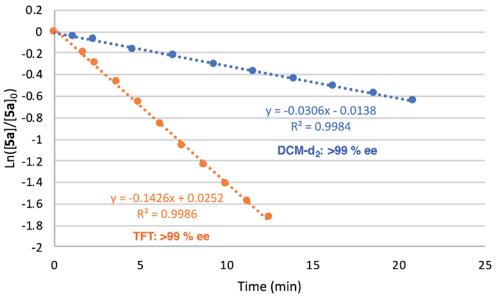

Fig. 9 Plot of Ln([**5a**]/[**5a**]$_0$) *vs.* time of model substrate **5a** to pyrrolidine **5b** *vs.* time (min) using (R_a,R_a,*S*,*S*)-**2**[NTf_2] at 0.5 mol%. Reactions conducted in DCM-d_2 or TFT (0.5 mL), [**5a**] = 0.6 M, [Ir] = 0.003 M. Conversion monitored using ^{1}H NMR.

2.5 Catalytic results for indoline-type products

With this overall improved catalyst/solvent system, we turned our attention to a challenging substrate of particular interest (**29a**), which would furnish the model 2-methylated indoline product **29b** upon successful hydroamination. Such substituted indoline motifs are found in many pharmaceutical compounds,[2] with the 2-methyl derivative featuring prominently in the anti-hypertensive/diuretic drug indapamide (as racemate) and in various potential anti-cancer drugs, among them the selective PI3Kβ inhibitor SAR-260301.[35] Not surprisingly then, a wide range of synthetic strategies have been developed for the asymmetric synthesis of these structures. Methods include the asymmetric hydrogenation of indole precursors,[36] or directly using indoline starting materials and accessing optically pure compounds *via* kinetic resolution strategies.[37] Constructing the indoline unit *via* ring-closing of appropriate precursors has also been explored, and formal hydroaminations with chiral copper catalysts have been described by both Chemler and Buchwald.[11b,38]

Fig. 10 shows hydroamination results as applied to model substrate **29a**, again recorded both in DCM-d_2 and TFT. When raising the catalyst loading to 5 mol% **2**[NTf_2], full conversion of **29a** to the indoline product **29b** was observed in both solvents at room temperature. Comparing the two solvents led to a similar increase in reaction rate as observed for pyrrolidine-type substrates when switching from DCM to TFT (k_{obs} = 0.83 × 10^{-2} to $k_{obs} = 3.4 \times 10^{-2}$, *i.e.* a 4-fold increase). More importantly, the already high enantioselectivity recorded in DCM-d_2 (90% ee) was substantially improved in TFT (95% ee), equating to more than doubling the ratio of the preferred enantiomer of **29b**.

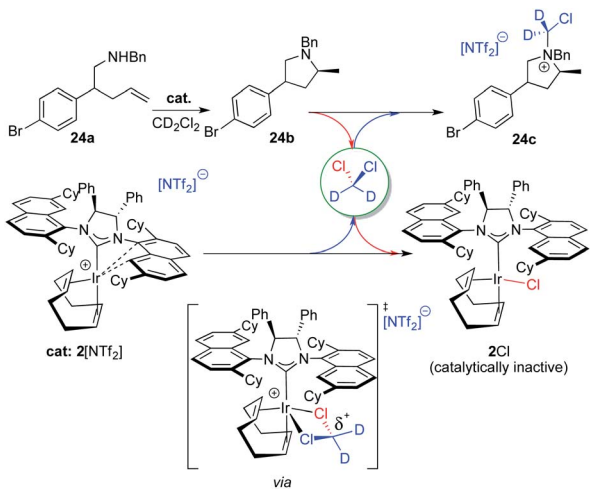

Fig. 8 Proposed deactivation pathway for **2**[NTf_2], forming **24c** and **2**Cl *via* the intermediate shown.

Table 2 gives an overview of results for 2-methylated indoline synthesis *via* our asymmetric HA protocol catalyzed by **2**[NTf_2]. The *para*-position of the starting aniline substrate was systematically varied with both electron-rich and electron-poor substituents. Data indicate that there is a clear electronic trend favoring cyclization of electron-rich aniline substrates.

TOF_{50} values reflect this, ranging from 6.3 h^{-1} (for **33a**) to 55.1 h^{-1} (**31a**) and 62.7 h^{-1} (**30a**). Electron-poor substituents such as **34a** and **35a** did not react at room temperature. Under slight heating (60 °C), cyclization did occur but a competing side reaction involving isomerization of the double bond yielded lower than expected amounts of product (**34b** and **35b**).

Trends in enantioselectivity were similar, with excellent results obtained for **29b** to **33b** (95–97% ee), while an erosion of optical purity was observed for **34b** and **35b**. A brief survey on the substitution pattern of the aniline core showed mixed outcomes with no apparent trends. Methyl substitution in both *ortho* and *meta* positions forms products **36b** and **38b** in excellent isolated yields and enantioselectivities, while a fluoro-substitution in the same positions proceeded smoothly, but led to drastically lower optical purity of the products (**37b**, **39b**). Results for **38b** are noteworthy for the fact that the speed of reaction is dramatically increased, a result also reflected by the *ortho*-substituted naphthyl-type substrate **40a**. How and why catalytic turnover is facilitated for these substrates is currently unknown, as is the reason for the drop in enantioselectivity when going from **38b** to **40b**.

2.6 Catalytic results for six-membered N-heterocyclic products

Results on classical asymmetric hydroamination protocols so far show that catalysts that produce 5-membered rings with high enantioselectivity (≥90% ee) fail to deliver 6-membered N-heterocycles with acceptable optical purity (or *vice versa*). Given our excellent results on cyclizing both pyrrolidine- and indoline-type substrates with **2**[NTf_2], we examined its performance with a small range of substrates that would deliver important 6-

Table 2 Cyclization of aminoolefins to give indolines using catalyst 2[NTf_2][a]

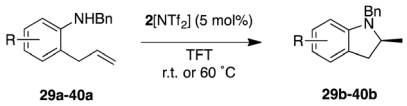

29a-40a 29b-40b

Product	29b	30b	31b	32b	33b	34b
	2mol%/5mol%					
ee (%)	95/95	96	97	97	96[c]	90[c,d,e]
Yield[b] (%)	97/99	83	87	99	58	68
k_{obs} (10^{-2} min^{-1})	1.7/3.3	6.2	7.1	1.9	0.5	—
TOF_{50} (h^{-1})	36.7/29.3	62.7	55.1	16.5	6.3	—

Product	35b	36b	37b	38b	39b	40b
ee (%)	72[c,d]	91	77	96	44	79
Yield (%)	45	83	89	96	87	99
k_{obs} (10^{-2} min^{-1})	—	1.9	0.1	59	0.6	27
TOF_{50} (h^{-1})	—	15.2	0.9	524	5.0	180

[a] Conditions: [anilino olefin] = 0.6 M, 5 mol% Ir cat., solvent = TFT and conducted at r.t. unless otherwise stated. All yields and ee values reported as an average of duplicate runs. [b] Isolated yield. [c] Only one run performed. [d] Reaction conducted at 60 °C. [e] ee determined *via* Mosher amide derivatization; single determination.

membered nitrogen-containing structures (Table 3). To do so, we evaluated substrates **41a** to **45a**, which upon cyclization would furnish the parent methylated piperidine (**41b**), tetrahydroisoquinoline (**42b**), tetrahydroquinoline (**43b**), tetrahydroquinoxaline (**44b**) or the corresponding methylated dihydro-1,4-benzoxazine (**45b**).

The three entries on the top row (**41b–43b**) showed high reactivity with full conversion to their products. Unfortunately, enantioselectivity for the formation of methylated piperidine **41b** was lower than for the analogous five-membered pyrrolidine (**5b**). Ring-expansion in the case of indoline-type substrates leads to tetrahydroquinoline **43b**, which in fact outperforms its five-membered sibling in terms of optical purity of the product (97% ee), although longer reaction times were required to obtain full conversion. In contrast, tetrahydroisoquinoline (**42b**) is formed almost instantaneously even at low temperature (<3 min), but does not show the same high selectivity observed for **43b** (74% ee).

The last two entries (**44b**, **45b**) underline the versatility of **2**[NTf_2] further as the catalyst is also able to perform the HA reaction to access heterocyclic rings with more than one heteroatom. Here, catalyst recognition appears to be crucial though, as we observe negligible enantioselectivity for **45b** (22% ee), whereas tetrahydroquinoxaline **44b** is produced with very high optical purity (90% ee).

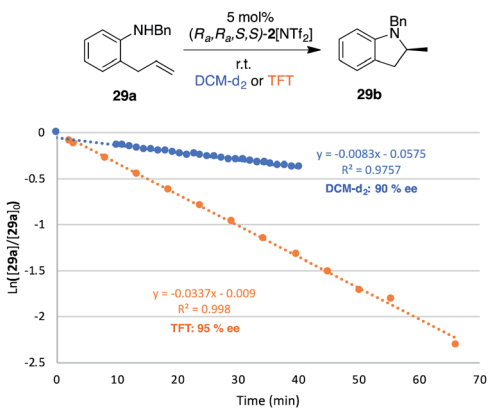

Fig. 10 Plot of Ln([**29a**]/[**29a**]$_0$) *vs.* time of substrate **29a** to indoline **29b** using (R_a,R_a,*S*,*S*)-**2**[NTf_2] at 5 mol%. Reactions conducted in DCM-d_2 or TFT (0.5 mL), [**29a**] = 0.6 M, [Ir] = 0.03 M. Conversion monitored using ^{1}H NMR.

2.7 Application of the HA reaction to access a pharmaceutically important molecule

The intramolecular hydroamination reaction has been modified and improved over the past 30 years in order to delimit the range of substrates available for such reactions with the ultimate aim being its incorporation into reaction schemes that access N-heterocycles of biological importance. To the best of our knowledge, not a single such application has been performed involving such a (asymmetric) hydroamination reaction.

The anti-tumor agent SAR-260301 (**48**), a pyrimidine indoline amide PI3Kβ inhibitor, was our synthetic target for investigation (Fig. 11). Prior research had shown that the (*S*)-configured

Table 3 HA of aminoolefins with 2[NTf_2] to give 6-membered rings[a]

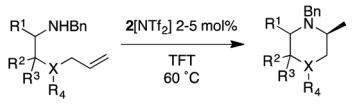

Product	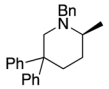	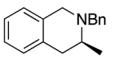	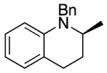
	41b	42b	43b
ee (%)	63	74[b]	97
Yield (%)	86	98	99

Product	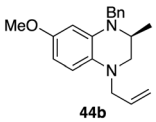	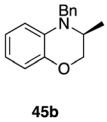
	44b	45b
ee (%)	90[c]	22
Yield (%)	27	56

[a] Conditions: [amine] = 0.6 M, 5 mol% Ir cat., solvent = TFT at 60 °C unless otherwise stated. All isolated yields and ee values reported are averages of at least two runs. [b] Reaction run at −9 °C. [c] Only one run performed.

indoline core is significantly more active than the (*R*)-enantiomer. The enantiomers were accessed in optically pure form after a classical preparative HPLC separation step using chiral stationary phases.[34c]

Direct access to SAR-260301 (**48**) was straightforward starting with the asymmetric hydroamination of **29a** using 2[NTf_2] to obtain the indoline core structure **29b**, followed by deprotection that furnished intermediate **46**. The last step involved amide bond formation by reacting **46** with sodium carboxylate **47** (synthesized from commercially available starting materials over 2 steps in 32% yield) according to the published protocol to directly furnish target compound (*S*)-SAR-260301 (**48**).

While we were not able to reproduce the reported yield for this last step (44% yield, reported yield for racemic **48:** 59%), we were nevertheless able to access (*S*)-**48** in 28% over only 3 linear steps from **29a**, with the high optical purity of **29b** being retained over the last two steps (see ESI† for details).[34d]

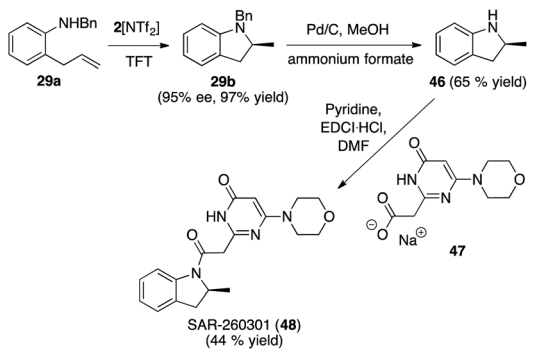

Fig. 11 Enantioselective synthesis of SAR-260301 (**48**).

With the above synthetic application, it becomes clear that the asymmetric hydroamination has potential as a synthetic methodology and with catalyst 2[NTf_2], we would now also be able to incorporate various functional groups into our indoline core and study the effect of these on the modified pharmacophores of **48** or related structures.

2.8 Experimental mechanistic investigations

A number of mechanistic pathways have been investigated for the hydroamination of alkenes. In terms of data available for group 9 metal catalysts, one of the two predominant catalytic cycles features an N–H oxidative addition, followed by insertion into the bound olefin and reductive elimination.[8b–d,39] This mechanism was uncovered for the intermolecular hydroamination reaction between norbornene or its derivatives and anilines. Mechanistic evidence for both rhodium and iridium catalyzed intramolecular hydroaminations point towards a distinct mechanism where initial olefin binding is followed by external attack of the amine onto the olefin to establish the C–N bond, with subsequent hydrogen transfer to the terminal alkene/alkyl position.[7d,e,12b,40,41]

Given that the present catalyst 2[NTf_2] is rather distinct from previously reported neutral iridium systems and given the fact that detailed mechanistic investigations of chiral HA catalysts are overall very rare,[3b,4a,6,42] we decided to gain insight into the mechanism at play with our catalyst system.

In addition, because the two major classes of starting materials and products shown above (Tables 1 and 2) feature electronically rather distinct amines (aliphatic for pyrrolidines, aromatic for indolines), we also believed that mechanistic data for both these substrate/product classes were required in order to guide the development of future classes of chiral HA catalysts.

Kinetic parameters were gathered for the HA of representative pyrrolidine educt **5a** and indoline precursor **29a** catalyzed by 2[NTf_2], with the reaction medium for all mechanistic investigations set to TFT as the solvent for the reasons cited above. Monitoring the disappearance and appearance of **5a**/**b** and **29a**/**b** resulted in pseudo-first order rate constants over the course of (typically) 2–3 half-lives (^{1}H NMR).

2.8.1 Kinetic order for pyrrolidine formation. Starting with the order for pyrrolidine formation (**5b**), various concentrations of [Ir] [3 to 9 mM (0.5–2.0 mol%)] were added to **5a** (0.6 M) in TFT at room temperature. Fig. 12a displays that a plot of reaction rate (k_{obs}) *versus* [Ir] was linear, indicating first-order kinetic dependence on catalyst. However, a non-linear least-squares fit to $f(x) = a[\mathrm{Ir}]^n$ resulted in an order (n) of 1.8, which seems to fit more with a second-order dependence of [Ir] than a first-order one (Fig. S4b, ESI†). However, it should be noted that a relatively high degree of error is associated with each of these pyrrolidine experiments as the reaction rates are unusually high under the conditions tested (2–10 minutes for 3 half-lives).

The kinetic order of pyrrolidine precursor **5a** was investigated subsequently by using a constant [Ir] (0.003 M) and various concentrations of **5a** (0.225–0.9 M). A decrease in

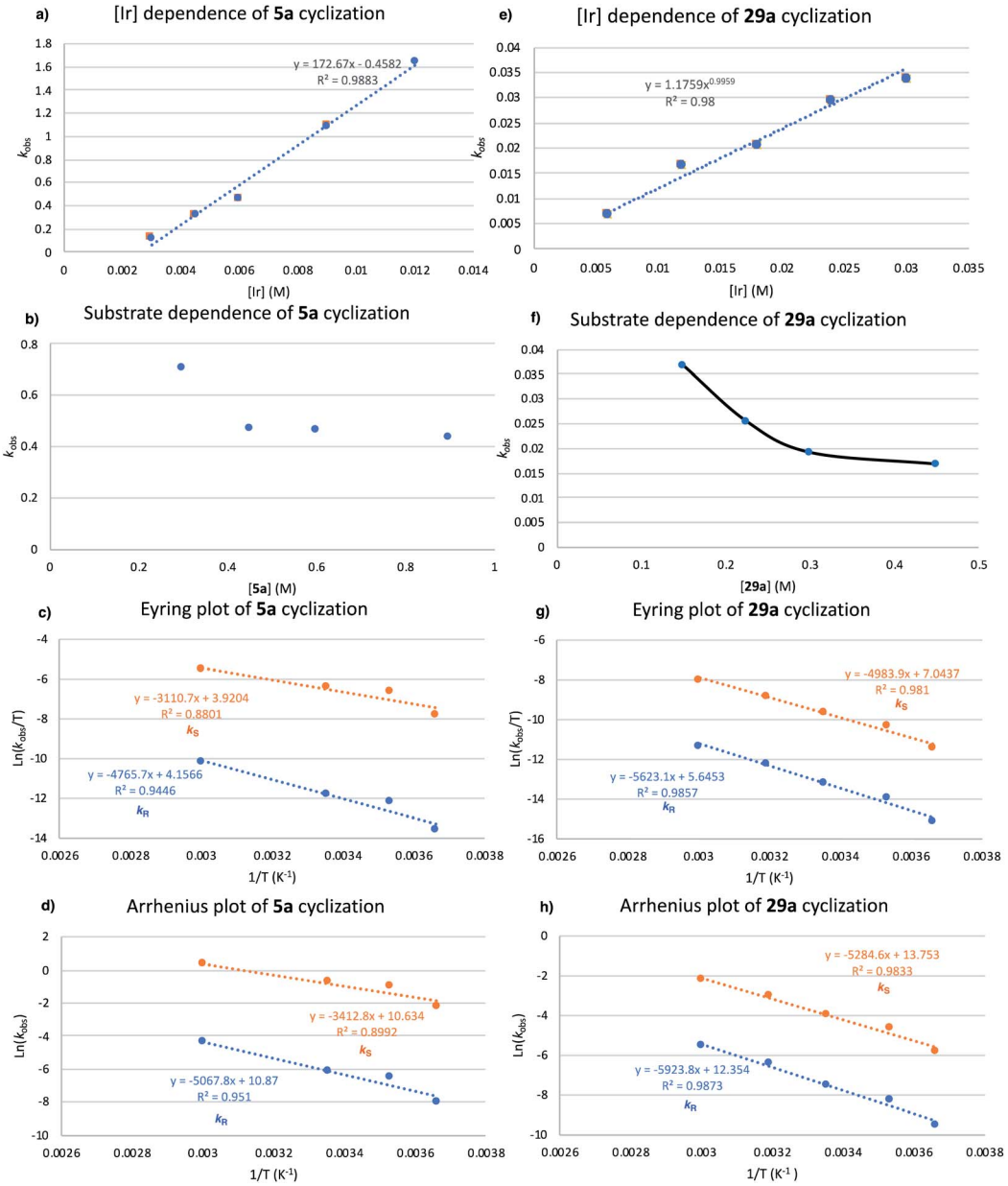

Fig. 12 (a) Relationship between k_{obs} and [**5a**] (TFT, 25 °C). Concentrations: [**5a**] = 0.6 M and [Ir] = 3 mM to 12 mM. (b) Relationship between k_{obs} and [**5a**] (TFT, 25 °C). Concentrations: [**5a**] = 0.225–0.9 M and [Ir] = 6 mM. (c) Eyring plot for the hydroamination of **5a** with **2**[NTf_2] (TFT, 0–60 °C). Concentrations: [**5a**] = 0.3 mM, [Ir] = 0.03 mM with ee values 98.2–99.4% over this temperature range. Rate constants k_R and k_S determined according to $k_R = k_{obs}(1 - ee)/2$ and $k_S = k_{obs}(1 + ee)/2$. (d) Arrhenius plot for HA of **5a** with **2**[NTf_2] [for conditions, see (c)]. (e) Relationship between k_{obs} and [Ir] for **29a** (TFT, 25 °C). Concentrations: [**29a**] = 0.6 M and [Ir] = 6 mM to 30 mM (f) relationship between k_{obs} and [**29a**] (TFT, 25 °C). Concentrations: [**29a**] = 0.15–0.45 M and [Ir] = 15 mM. (g) Eyring plot for HA of **29a** with **2**[NTf_2] (TFT, 0–60 °C). Concentrations: [**29a**] = 0.3 mM, [Ir] = 15 mM with ee values of 93.0–95.3% over this temperature range. Rate constants k_R and k_S were determined according to $k_R = k_{obs}(1 - ee)/2$ and $k_S = k_{obs}(1 + ee)/2$. (h) Arrhenius plot for HA of **29a** with **2**[NTf_2] [for conditions, see (g)].

reaction rate as initial substrate concentration increases was observed, which is consistent with an inverse order dependence of the rate of reaction on substrate concentration. Similar to our kinetic order dependence on catalyst, the data are not clear-cut, as substrate concentrations between 0.45-0.9 M all gave very similar k_{obs} values (Fig. 12b).

2.8.2 Activation parameters for pyrrolidines. A series of reactions were employed over a range of temperatures (0–60 °C) in order to obtain activation parameters for the hydroamination of **5a** with **2**[NTf_2]; pseudo-first order rate constants were extracted from linear plots of $[\mathbf{5a}]_t$ *versus* time for each temperature value. Activation parameters for the lower transition state to pyrrolidine (*S*)-**5b** ($\Delta H^{\ddagger}$ = 6.2 kcal mol^{-1}, $\Delta S^{\ddagger}$ = −39.4 cal K^{-1} mol^{-1}) and for the higher transition state (*R*)-**5b** ($\Delta H^{\ddagger}$ = 9.5 kcal mol^{-1}, $\Delta S^{\ddagger}$ = −38.9 cal K^{-1} mol^{-1}) were extracted from the Eyring plot (Fig. 12c). The diastereomeric

transition states have a difference of $\Delta\Delta H^{\ddagger} = 3.3$ kcal mol^{-1}, while the difference in order is $\Delta\Delta S^{\ddagger} = 0.5$ cal K^{-1} mol^{-1}, indicating very similarly ordered transition states for the formation of (*S*)-**5b** and (*R*)-**5b**.

The Arrhenius plot (Fig. 12d) generates activation energy values for the formation of the major enantiomer (*S*)-**5b** (E_a = 6.8 kcal mol^{-1}) and minor enantiomer (*R*)-**5b** (E_a = 10.1 kcal mol^{-1}). The difference in activation energy ΔE_a = 3.3 kcal mol^{-1} would correspond to product formation with an approximately 200 : 1 ratio of (*S*)-**5b** *versus* (*R*)-**5b**, which is fully consistent with our experimentally obtained results.

2.8.3 Kinetic order for indolines. Kinetic studies were repeated for the indoline precursor **29a**, with parameters as follows; [Ir] [6 to 30 mM (1.0–5.0 mol%)], and [**29a**] (0.6 M) in TFT at room temperature. Fig. 12e shows that a plot of reaction rate (k_{obs}) *versus* [Ir] was linear, again suggesting first-order kinetic dependence on the catalyst. In this case, a non-linear least-squares fit to $f(x) = a[\mathrm{Ir}]^n$ provided (n) of 1.0, clearly confirming first-order kinetics (Fig. S5b, ESI†).

Studies on the kinetic order of indoline precursor **29a** were performed next by using a constant [Ir] concentration (0.015 M) and systematically varying the concentration of **29a** from 0.15 to 0.45 M. Again, we notice a decreasing reaction rate as initial substrate concentration increases, as expected for an inverse order dependence reaction rate from the substrate concentration (Fig. 12f).

2.8.4 Activation parameters for indolines. Subsequently, the activation parameters for the hydroamination of **29a** with **2**[NTf_2] were obtained over an extended temperature range (0–60 °C); pseudo-first order rate constants were again derived from linear plots of [**29a**]$_t$ *versus* time for each temperature value. The activation parameters for the lower transition state to indoline (*S*)-**29b** ($\Delta H^{\ddagger} = 9.7$ kcal mol^{-1}, $\Delta S^{\ddagger} = -33.2$ cal K^{-1} mol^{-1}) and for the higher transition state (*R*)-**29b** ($\Delta H^{\ddagger} = 11.2$ kcal mol^{-1}, $\Delta S^{\ddagger} = -36$ cal K^{-1} mol^{-1}) were once more extracted from the Eyring plot (Fig. 12g). In the case of these indolines, the diastereomeric cyclization transition states have a difference of $\Delta\Delta H^{\ddagger} = 1.5$ kcal mol^{-1}, while the difference in order is $\Delta\Delta S^{\ddagger} = 2.8$ cal K^{-1} mol^{-1}, indicating a slightly more ordered transition state for formation of (*S*)-**29b**.

Activation energy values were generated from the Arrhenius plot (Fig. 12h) for the formation of the major enantiomer (*S*)-**29b** ($E_a = 10.5$ kcal mol^{-1}) and minor enantiomer (*R*)-**29b** (E_a = 11.8 kcal mol^{-1}). The difference in activation energy ΔE_a = 1.3 kcal mol^{-1} equates to an approximately 10 : 1 (*S*) *versus* (*R*) ratio of the respective enantiomers, therefore slightly undervaluing the recorded enantioselectivity for **29b** (95% ee).

2.8.5 Hammett study (indoline-type). The rate of the **2**[NTf_2]-catalyzed asymmetric hydroamination reaction of **29a–33a** (see Table 2), *i.e.* the substrates that undergo HA at room temperature, was plotted as a function of the *para*-substituent on the 2-allyl aniline starting materials (Fig. 13). The conversion of **29a–33a** to **29b–33b** in the presence of 5 mol% **2**[NTf_2] was followed by ^{1}H NMR to obtain reaction rates. The Hammett plot gave a very large, negative ρ value of −4.5.

It is tempting to assume that this arises from the build-up of a positive charge on the nitrogen following its attack onto the olefin. This would then mean that such an olefin activation mechanism is rather more likely than the amine-OA pathway, where work by Brookhart has seen the opposite electronic trend.[43]

2.8.6 Kinetic isotope studies. Model pyrrolidine substrate **5a** and indoline substrate **29a** were monodeuterated at the nitrogen in order to gain an understanding of the turnover-limiting step of the mechanism through evaluation of the H/D kinetic isotope effect (KIE, Fig. 14). The pseudo-first order plots (see ESI Fig. S7†) of the cyclization of **5a** and **5a**-d_1 in TFT at room temperature provided k_{obs} values of 0.31 and 0.092 respectively, resulting in a primary KIE (3.37). For the indoline substrate, pseudo-first order plots of **29a** and **29a**-d_1 (see ESI Fig. S8†) resulted in k_{obs} values of 0.033 and 0.0195 respectively and a smaller primary KIE (1.69). For both of these substrate classes, these results imply that breaking of the N–H bond or subsequent breaking of the Ir–H bond are part of the rate-determining step. Taken together with results from our Hammett study, the classical hydroamination pathway with initial oxidative addition of the amine (and subsequent insertion + reductive elimination) can be ruled out for indoline type substrates and appears highly unlikely for pyrrolidines as well. The difference in KIE values between **5a** and **29a** indicates that these two substrate classes go *via* transition states with differing degrees of linearity.[44]

2.8.7 Summary of kinetic experiments. Kinetic analysis of the **2**[NTf_2] catalyzed asymmetric intramolecular hydroamination to produce methylated pyrrolidine **5b** and methylated indoline **29b** has revealed first order dependance on [Ir] and inverse order dependance with respect to both substrate [**5a**] and [**29a**]. The difference in activation energies leading to (*R*) or (*S*) product ($\Delta E_a = 3.3$ kcal mol^{-1} for **5b**, ΔE_a = 1.3 kcal mol^{-1} for **29b**) generated from Arrhenius plots is reasonably consistent with experimental ee values (>99% ee for **5b**, 95% ee for **29b**). The Hammett study on appropriately *para*-substituted derivatives of **29a** gave a large negative ρ value, indicating that electron donating groups speed up the reaction, a result in line with a mechanism involving external attack of the amine onto the coordinated olefin with concomitant charge build-up and subsequent formation of an ammonium cation. Finally, values recorded from the kinetic isotope effect analysis ($k_H/k_D = 3.37$ for **5b**, $k_H/k_D = 1.69$ for **29b**) suggest that a primary KIE is involved for both substrate classes. This means that

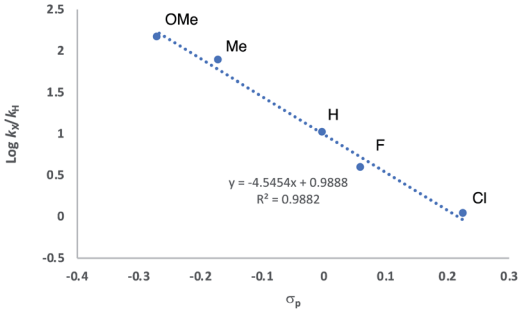

Fig. 13 Hammett plot for HA of anilines **29a–33a** with **2**[NTf_2] (TFT, 25 °C). Concentrations: [**29a–33a**] = 0.6 M and [Ir] = 0.03 M.

breaking of the N–H (or Ir–H) bond is part of the turnover-limiting step (TLS).

While Hammett studies as well as KIEs clearly point towards a mechanism of nucleophilic amine attack followed by proton migration and product liberation, the lack of spectroscopic evidence of any catalytic intermediates and our inability to clearly differentiate the TLS led us to examine the mechanism of the reaction further *via* DFT calculations.

2.9 Computational mechanistic investigations

The reaction mechanism catalyzed by **2**[NTf_2] has been theoretically investigated for **18a** and **29a** as representative classes of pyrrolidine and indoline precursors.

2.9.1 Reactivity of the pyrrolidine-type substrate. As reported above, the catalytic cycle occurring under the reaction conditions can involve either the initial activation of the olefin functionality (C=C bond activation pathway) or of the amine functionality (N–H bond activation pathway, see Scheme S1†).

At first, we explored the different ways of substrate coordination to the catalytically active species **A** (14-electron complex without naphthyl-Ir stabilization), and we localized the three structures **B1** (alkene coordination), **B2** (nitrogen coordination) and **B3** (aminoolefin coordination) reported in Fig. 15. Both olefin coordination and nitrogen lone pair coordination to the metal, **B1** and **B2**, are energetically favored, with the nitrogen adduct (**B2**) being 5.2 kcal mol^{-1} more stable than **A** and the alternative alkene adduct **B1** being 1 kcal mol^{-1} higher in energy with respect to **B2**. Finally, the chelating aminoalkene **B3** coordination is disfavored by 13.4 kcal mol^{-1} due to the crowded coordination environment at the metal center.

2.9.2 Olefin activation pathway. Starting from intermediate **B1**, the amine can approach the olefin functionality in the C–N bond formation step through different trajectories, leading to the simultaneous formation of two chiral centers (one on the expected carbon atom of the substrate, and the other one on the nascent ammonium ion). The resulting four diastereomeric Ir^{I} cycloammonio-alkyl intermediates **C1–C4** are in dynamic equilibrium, as depicted in Scheme 1. These ring closure steps are reversible, as all routes are calculated to be energetically viable (starting from **B1** the barriers leading to **C1–C4** are all around 7–9 kcal mol^{-1}). Consequently, transient diastereomers will finally accumulate into the most favored (S_C, R_N) **C1** configuration, lying at −6.8 kcal mol^{-1}.

The following step, corresponding to the hydrogen transfer from the ammonium ion to the iridium, leads to formation of the transient Ir^{III}-hydride intermediates **D1–D2**. These intermediates bear only one chiral center on the carbon atom, with *R* and *S* configuration, respectively. The energy barriers for the favored **C–D** transition states leading to the **D1** and **D2** intermediates are 14.3 and 19.4 kcal mol^{-1} from the (S_c, R_N) **C1** and (R_c, S_N) **C2** diastereoisomers, respectively.

The alternative routes (light blue and dark red profiles in Scheme 1) starting from the other two diastereomers (with opposite absolute stereochemistry on nitrogen) were ruled out, since they require much higher energy barriers, *i.e.* 32.2 and 27.8 kcal mol^{-1} from the (S_c, S_N) **C3** and (R_c, R_N) **C4** diastereoisomers, respectively. Formation of the resulting intermediates **D1** and **D2** is calculated to be endothermic with respect to the most stable Ir^{I} cycloammonio-alkyl intermediates **C1** and **C2**. The reaction is completed by reductive elimination corresponding to the H transfer from the Ir center to the Ir-bound terminal CH_2 group of the substrate, with formation of the desired product and regeneration of the catalyst. Overall, the **D** → **E** step is straightforward as it requires overcoming a relative small energy barrier, lower than 10 kcal mol^{-1} for both the S_c and R_c isomers. Formation of product **E** is thermodynamically favored by almost 10.0 kcal mol^{-1} over starting material **A**. It is worth noting that the H transfer step (**C** → **D**) is required to facilitate the subsequent reductive elimination step. In fact, all of our attempts to localize a direct hydrogen transfer **C** → **E** failed.

On the basis of these mechanistic results, the rate-determining step involves an H transfer reaction, which is in agreement with the experimentally determined KIE results. Nevertheless, the rate-determining step involves a different transition state along the two pathways that lead to the formation of the respective enantiomers. For the formation of the *R*-configured product, the initial ammonium to metal hydrogen transfer (**C2–D2**) at 12.6 kcal mol^{-1} represents the RDS, while for formation of the preferred *S* product, it is the subsequent reductive elimination step (**D1–E1**) at 8.3 kcal mol^{-1} that is minimally higher than transformation **C1–D1**.

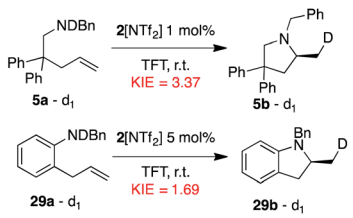

Fig. 14 Determination of KIE values for **5a** and **29a**.

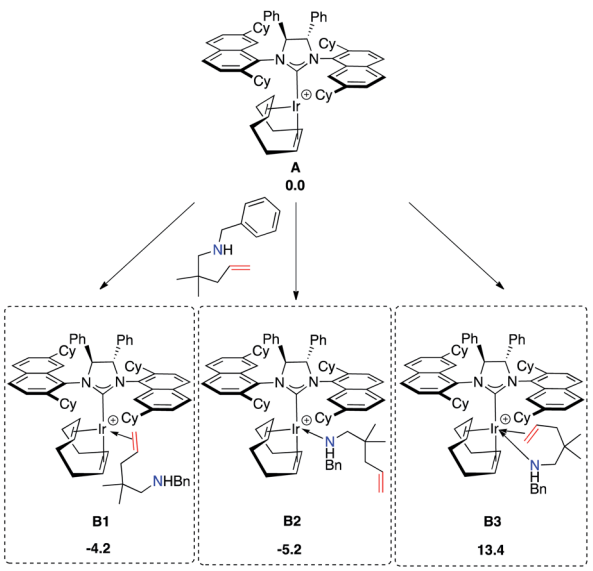

Fig. 15 Coordination modes of the substrate to Ir (kcal mol^{-1}).

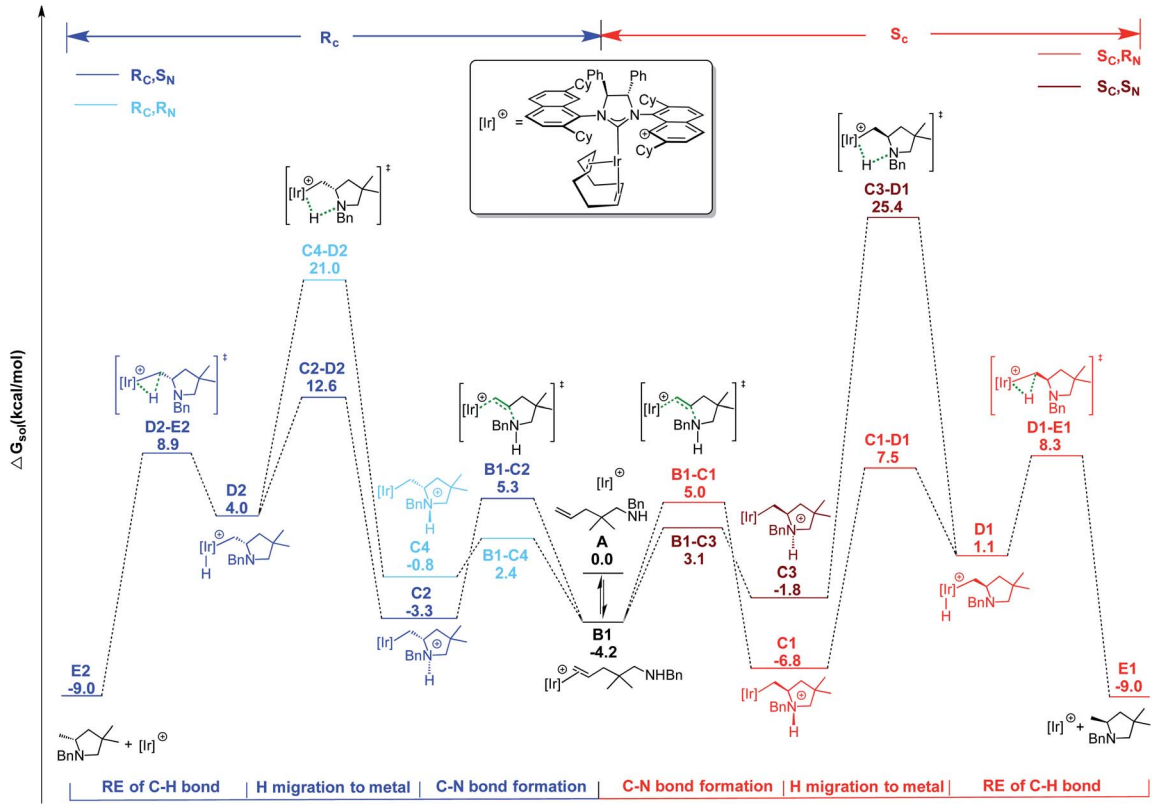

Scheme 1 Energy profile for C=C bond activation pathway for HA of pyrrolidine precursor **18a** with catalyst **2**. Free energies in kcal mol^{-1}.

Overall, $\Delta\Delta G^{\neq}_{S-R}$ is calculated to be 4.3 kcal mol^{-1} in favor of the formation of the S_c enantiomer, in agreement with the high enantioselectivity emerging from the experiments. For an easier analysis, in the following we compare the geometries of the two competing **C–D** transition states since we retain that the steric scenario is rather similar in **C–D** and subsequent **D–E** steps.

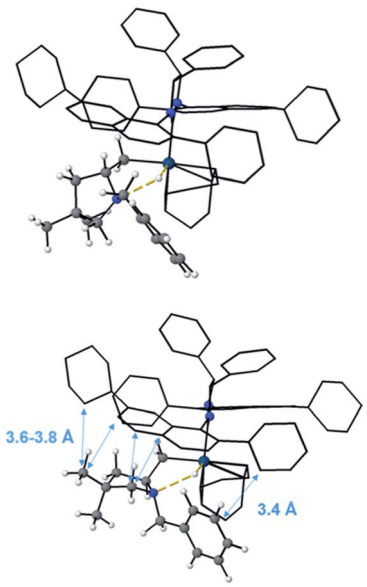

Fig. 16 Optimized geometries of the **C–D** (S_c, R_N) and **C–D** (R_c, S_N) transition states.

The geometries reported in Fig. 16 highlight that the steric hindrance of the catalyst seems to play a key role in the enantioselection of the product formed due to repulsive interactions between the substrate and the naphthyl rings as well as the cyclohexyl groups on the ligand. The geminal methyls and the phenyl group on aminoalkene **18** are placed away from the NHC-ligand in the favored pathway, leading to the S_c product (Fig. 16, top), while several unfavorable short distances between the NHC-ligand and the aminoalkene are found in structures along the R_c pathway (Fig. 16, bottom).

2.9.3 N–H bond activation pathway. The alternative N–H bond activation pathway, starting from the coordination intermediate **B2**, has also been explored (see Scheme S2†) for the formation of the experimentally favored *S* product.

The unfavored thermodynamic of the intermediates involved, together with unaffordable energy barriers for the initial N–H bond activation step (50.5 kcal mol^{-1}) and the following olefin insertion into the Ir–N bond (61.5 kcal mol^{-1}), mean that this pathway can be ruled out.

2.9.4 Reactivity of the indoline-type substrate. The favored olefin activation pathway for substrate **29a** is reported in Scheme 2. As already discussed, the catalytic cycle begins with the nucleophilic attack of the nitrogen on the olefin functionality in species **B1**, lying 1.6 kcal mol^{-1} below **A**. Differently from substrate **18b**, and the results reported in Scheme 1, the C–N bond formation step is endothermic for all four diastereomers,

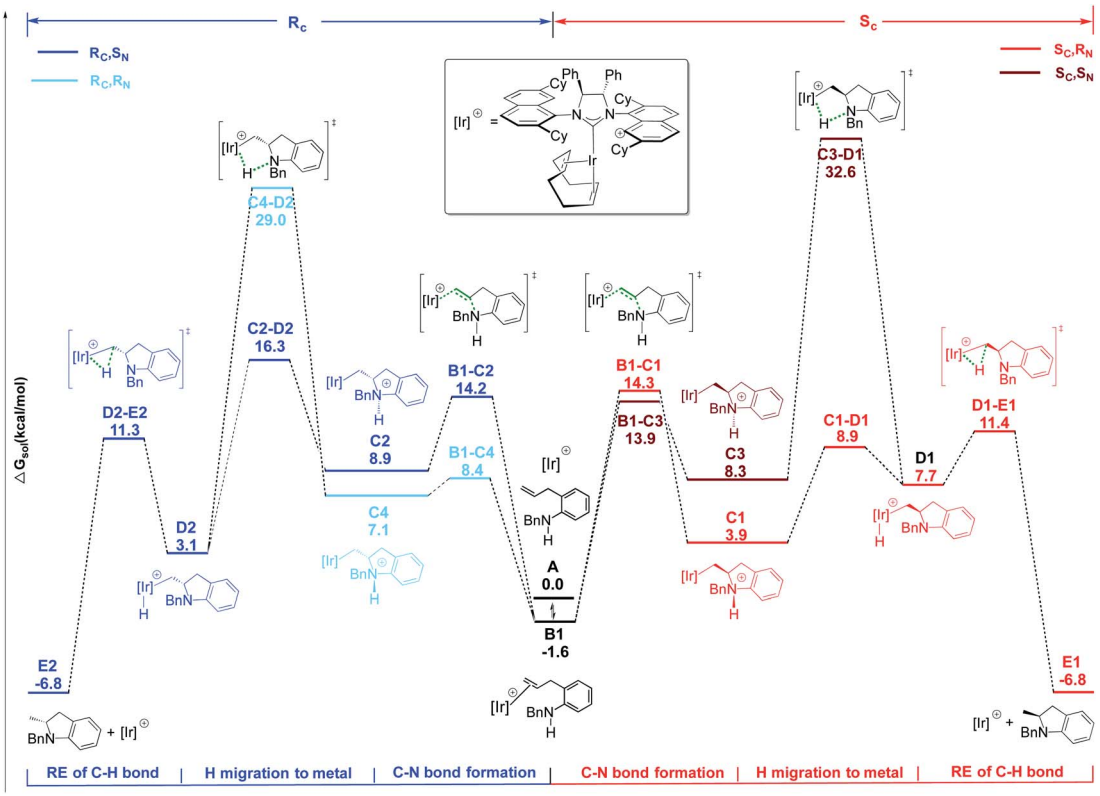

Scheme 2 Energy profile for C=C activation pathway for HA reaction of indoline **29a** in the presence of **2**. Free energies in kcal mol^{-1}.

and requires overcoming an energy barrier ranging from 10 to 16 kcal mol^{-1} for the different pathways.

The Ir–C bond cleavage proceeds again *via* a stepwise mechanism including the proton transfer to the Ir center (**C** → **D**) followed by a C–H reductive elimination step (**D** → **E**). As observed for **18a**, only two pathways are energetically affordable, which are those passing through transition states **C1–D1** and **C2–D2** (see Scheme 2). The high energy barrier of 34.2 and 30.6 kcal mol^{-1} required to reach transition states **C3–D1** and **C4–D2**, respectively, allows us to rule out these two alternative pathways.

Formation of the two enantiomeric products is determined by different steps: the ring closure step *via* transition state **B1–C1**, requiring a barrier of 15.9 kcal mol^{-1} for the formation of a S_C center, with the following proton transfer being easy; on the contrary, the first proton transfer step, *via* transition state **C2–D2**, is rate determining for the formation of the R_C center, requiring a barrier of 17.9 kcal mol^{-1}. The calculated $\Delta\Delta G^{\neq}$ of 2.0 kcal mol^{-1} indicates a clear preference for the formation of the S_C isomer, in agreement with experiments. The different nature of the determining transition states along the two pathways for **29a** nicely matches with the different entropic contributions measured by kinetic experiments for the formation of the two enantiomers (see above).

3. Conclusions

Two decades after Togni *et al.* had shown that neutral iridium catalysts containing chelating diphosphines can effect the asymmetric hydroamination between norbornene and aniline, we report the development of cationic iridium systems of general formula [(NHC*)Ir(COD)][X] that are able to cyclize unactivated aminoalkenes with unprecedented ease. Particularly noteworthy features of these new catalysts are the incorporation of a chiral, (monodentate) NHC steering ligand (a first in this chemistry) as well as the use of the NTf_2 anion, again a moiety that despite the popularity of cationic iridium catalysts in catalysis has no precedence in the iridium literature.

Hydroamination products that can be obtained include a range of highly enantioenriched methylated pyrrolidines and indolines as representatives of five-membered N-heterocycles (≥95% ee). The same catalyst system **2**[NTf_2] can also be used for the construction of tetrahydroquinolines and tetrahydroquinoxaline, where we again see formation of products in high optical purity (≥90% ee). Other 6-membered heterocycles such as tetrahydroisoquinolines or dihydro-1,4-benzoxazine are produced just as easily, but are not obtained with the same level of enantioselectivity.

The present catalytic system not only shows a rather broad range of applicability, but also stands out as it is the first late-transition metal system that easily matches and exceeds intramolecular HA results obtained in the past with chiral early-transition or lanthanide based systems. It therefore means that it is now possible to incorporate important functional groups (*e.g.* carbonyl-containing FG) into substrates, rendering the present protocol more amenable to its incorporation into synthetic strategies of more complex organic molecules. To underline the validity of **2**[NTf_2] as a catalyst in this context, we

employed it to access a pharmaceutical compounds in optically enriched form, namely SAR-260301, an anti-tumor agent that acts as a PI3Kβ inhibitor. As far as we are aware, it is the first asymmetric synthesis of SAR-260301 and the first example where the classical hydroamination reaction is employed to access a pharmaceutically relevant molecule or natural product.

In the quest to understand the exact role of the catalyst and in view of future developments of the platform, we conducted a comprehensive experimental and computational investigation on the system. These studies have furnished important results with regards to both individual reaction steps of the catalytic cycle as well as mode of enantioselection with the **2**[NTf_2] catalyst.

Collectively, the results of the investigations indicate that these asymmetric intramolecular hydroamination reactions commence with coordination of the olefin functionality to the catalytically active 14-electron iridium species. The catalytic mechanism proceeds *via* the following fundamental steps: (1) smooth and reversible ring-closure through external amine attack, resulting in formation of the C–N bond; (2) proton migration from the ammonium unit of the formed zwitterionic intermediate to the metal center, followed by (3) C–H reductive elimination affording the desired N-heterocyclic product. The nature of the rate-determining transition state (H migration to iridium) is in agreement with the experimentally measured KIE parameters for both pyrrolidine-type and indoline-type substrates.

On the other hand, the high enantioselectivities, as measured experimentally from the difference in activation energies generated from Arrhenius plots, was further validated and explained by our *in silico* studies. These ascribed such energetic differences to repulsive interactions between the substrate and the naphthyl rings on the ligand in the unfavored reaction pathways leading to the (*R*)-configured product, indeed a result that is again in line with the experimental outcome for substrates **23–25**, where the erosion of enantioselectivity must come from similar repulsion when accessing the respective diastereomers. Such repulsive steric interactions also seem responsible for the pronounced effects that the various substituents have when performing the asymmetric intramolecular hydroamination on indoline-type substrates.

We are therefore confident that heterocycles that at present (with **2**[NTf_2]) cannot be produced in high optical purity will be accessible. With the in depth study provided here, we are now in a position where computational modeling can be performed before modifying and fine-tuning the steric bulk of our chiral NHC ligand. These studies and related investigations are ongoing.

Conflicts of interest

There are no conflicts to declare.

Acknowledgements

D. F. and P. G. thank UWA for a Research Training Postgraduate (RTP) Scholarship. G. S. thanks UWA for an International Postgraduate Research Scholarship (IPRS). R. D. thanks the Australian Research Council for generous funding (FT130101713).

Notes and references

1 For relevant and selected reviews, see: (*a*) T. E. Müller, K. C. Hultzsch, M. Yus, F. Foubelo and M. Tada, *Chem. Rev.*, 2008, **108**, 3795–3892; (*b*) J. Hannedouche and E. Schulz, *Chem.–Eur. J.*, 2013, **19**, 4972–4985; (*c*) L. Huang, M. Arndt, K. Gooßen, H. Heydt and L. J. Gooßen, *Chem. Rev.*, 2015, **115**, 2596–2697; (*d*) E. Bernoud, C. Lepori, M. Mellah, E. Schulz and J. Hannedouche, *Catal. Sci. Technol.*, 2015, **5**, 2017–2037; (*e*) C. Michon, M.-A. Abadie, F. Medina and F. Agbossou-Niedercorn, *J. Organomet. Chem.*, 2017, **847**, 13–27; (*f*) J. Hannedouche and E. Schulz, *Organometallics*, 2018, **37**, 4313–4326.

2 E. Vitaku, D. Smith and J. Njardarson, *J. Med. Chem.*, 2014, **57**, 10257–10274.

3 (*a*) M. R. Gagné, L. Brard, V. Conticello, M. A. Giardello, C. L. Stern and T. J. Marks, *Organometallics*, 1992, **11**, 2003–2005; (*b*) M. A. Giardello, V. P. Conticello, L. Brard, M. R. Gagné and T. J. Marks, *J. Am. Chem. Soc.*, 1994, **116**, 10241–10254.

4 (*a*) D. V. Gribkov, K. C. Hultzsch and F. Hampel, *J. Am. Chem. Soc.*, 2006, **128**, 3748–3759; (*b*) A. L. Reznichenko, H. N. Nguyen and K. C. Hultzsch, *Angew. Chem., Int. Ed.*, 2010, **49**, 8984–8987; (*c*) A. L. Reznichenko, T. J. Emge, S. Audörsch, E. G. Klauber, K. C. Hultzsch and B. Schmidt, *Organometallics*, 2011, **30**, 921–924; (*d*) For an overview of early lanthanide catalyzed hydroamination: S. Hong and T. J. Marks, *Acc. Chem. Res.*, 2004, **37**, 673–686.

5 M. C. Wood, D. C. Leitch, C. S. Yeung, J. A. Kozak and L. L. Schafer, *Angew. Chem., Int. Ed.*, 2007, **46**, 354–358.

6 (*a*) K. Manna, S. Xu and A. D. Sadow, *Angew. Chem., Int. Ed.*, 2011, **50**, 1865–1868; (*b*) K. Manna, W. C. Everett, G. Schoendorff, A. Ellern, T. L. Windus and A. D. Sadow, *J. Am. Chem. Soc.*, 2013, **135**, 7235–7250; (*c*) K. Manna, N. Eedugurala and A. D. Sadow, *J. Am. Chem. Soc.*, 2015, **137**, 425–435.

7 (*a*) X. Shen and S. L. Buchwald, *Angew. Chem., Int. Ed.*, 2010, **49**, 564–567. For reaction development and mechanistic insights of non-chiral cationic rhodium systems, see: (*b*) A. Takemiya and J. F. Hartwig, *J. Am. Chem. Soc.*, 2006, **128**, 6042–6043; (*c*) Z. Liu and J. F. Hartwig, *J. Am. Chem. Soc.*, 2008, **130**, 1570–1571; (*d*) L. D. Julian and J. F. Hartwig, *J. Am. Chem. Soc.*, 2010, **132**, 13813–13822; (*e*) Z. Liu, H. Yamamichi, S. T. Madrahimov and J. F. Hartwig, *J. Am. Chem. Soc.*, 2011, **133**, 2772–2782.

8 (*a*) R. Dorta, P. Egli, F. Zürcher and A. Togni, *J. Am. Chem. Soc.*, 1997, **119**, 10857–10858; (*b*) J. Zhou and J. F. Hartwig, *J. Am. Chem. Soc.*, 2008, **130**, 12220–12221; (*c*) S. Pan, K. Endo and T. Shibata, *Org. Lett.*, 2012, **14**, 780–783; (*d*) C. S. Sevov, J. Zhou and J. F. Hartwig, *J. Am. Chem. Soc.*, 2014, **136**, 3200–3207; (*e*) E. P. Vanable, J. L. Kennemur, L. A. Joyce, R. T. Ruck, D. M. Schultz and K. L. Hull, *J. Am. Chem. Soc.*, 2019, **141**, 739–742.

9 For selected recent examples of (asymmetric) LTM catalyzed intermolecular HA with activated olefin substrates: (*a*) M. L. Cooke, K. Xu and B. Breit, *Angew. Chem., Int. Ed.*, 2012, **51**, 10876–10879; (*b*) N. J. Adamson, E. Hull and S. J. Malcolmson, *J. Am. Chem. Soc.*, 2017, **139**, 7180–7183; (*c*) S. Kim, T. Wurm, G. A. Brito, W. Jung, J. R. Zbieg, C. E. Stivala and M. J. Krische, *J. Am. Chem. Soc.*, 2018, **140**, 9087–9090.

10 For formal intermolecular HA reactions with these systems, see: (*a*) Y. Miki, K. Hirano, T. Satoh and M. Miura, *Angew. Chem., Int. Ed.*, 2013, **52**, 10830–10834; (*b*) S. Zhu, N. Niljianskul and S. Buchwald, *J. Am. Chem. Soc.*, 2013, **135**, 15746–15749; (*c*) Y. Miki, K. Hirano, T. Satoh and M. Miura, *J. Am. Chem. Soc.*, 2014, **16**, 1498–1501; (*d*) J. Bandar, M. Pirnot and S. Buchwald, *J. Am. Chem. Soc.*, 2015, **137**, 14812–14818; (*e*) M. Pirnot, Y. Wang and S. Buchwald, *Angew. Chem., Int. Ed.*, 2016, **55**, 48–57; (*f*) Y. Xi, T. Butcher, J. Zhang and J. Hartwig, *Angew. Chem., Int. Ed.*, 2016, **55**, 776–780; (*g*) S. Ichikawa, S. Zhu and S. Buchwald, *Angew. Chem., Int. Ed.*, 2018, **57**, 8714–8718.

11 For similar asymmetric intramolecular HA reactions with Cu systems, see: (*a*) P. Fuller, J. Kim and S. Chemler, *J. Am. Chem. Soc.*, 2008, **130**, 17638–17639; (*b*) B. Turnpenny, K. Hyman and S. Chemler, *Organometallics*, 2012, **31**, 7819–7822; (*c*) H. Wang, J. Yang and S. Buchwald, *J. Am. Chem. Soc.*, 2017, **139**, 8428–8431.

12 (*a*) K. D. Hesp and M. Stradiotto, *Org. Lett.*, 2009, **11**, 1449–1452; (*b*) K. D. Hesp, S. Tobisch and M. Stradiotto, *J. Am. Chem. Soc.*, 2010, **132**, 413–426.

13 K. D. Hesp, R. McDonald and M. Stradiotto, *Can. J. Chem.*, 2010, **88**, 700–708.

14 For our first contribution, see: (*a*) R. Mariz, X. Luan, M. Gatti, A. Linden and R. Dorta, *J. Am. Chem. Soc.*, 2008, **130**, 2172–2173. For a more recent review, see: (*b*) G. Sipos, E. E. Drinkel and R. Dorta, *Chem. Soc. Rev.*, 2015, **44**, 3834–3860.

15 E. E. Drinkel, PhD thesis, University of Zurich, 2011, ch. 3, pp. 69–93.

16 (*a*) C. Y. Tang, A. L. Thompson and S. Aldridge, *J. Am. Chem. Soc.*, 2010, **132**, 10578–10591; (*b*) C. Y. Tang, J. Lednik, D. Vidovic, A. L. Thompson and S. Aldridge, *Chem. Commun.*, 2011, **47**, 2523–2525.

17 For early contributions from our group, see: (*a*) X. Luan, R. Mariz, M. Gatti, C. Costabile, A. Poater, L. Cavallo, A. Linden and R. Dorta, *J. Am. Chem. Soc.*, 2008, **130**, 6848–6858; (*b*) X. Luan, R. Mariz, C. Robert, M. Gatti, S. Blumentritt, A. Linden and R. Dorta, *Org. Lett.*, 2008, **10**, 5569–5572; (*c*) L. Vieille-Petit, X. Luan, R. Mariz, S. Blumentritt, A. Linden and R. Dorta, *Eur. J. Inorg. Chem.*, 2009, **13**, 1861–1870.

18 G. Sipos, A. Ou, B. Skelton, L. Falivene, L. Cavallo and R. Dorta, *Chem.–Eur. J.*, 2016, **22**, 6939–6946.

19 P. Gao, G. Sipos, D. Foster and R. Dorta, *ACS Catal.*, 2017, **7**, 6060–6064.

20 In many other ligand designs, the fused cyclohexyl motif has proven successful (*e.g.* salen-type ligands, Trost ligands). The few reports on NHCs featuring this unit have shown disappointing selectivities (4–23% ee), see ref. [17b] and: (*a*) T. J. Seiders, D. W. Ward and R. H. Grubbs, *Org. Lett.*, 2001, **3**, 3225–3228; (*b*) S. Lee and J. F. Hartwig, *J. Org. Chem.*, 2001, **66**, 3402–3415; (*c*) T. Arao, K. Sato, K. Kondo and T. Aoyama, *Chem. Pharm. Bull.*, 2006, **54**, 1576–1581; (*d*) R. Lai, J.-C. Daran, A. Heumann, A. Zaragori-Benedetti and E. Rafii, *Inorg. Chim. Acta*, 2009, **362**, 4849–4852.

21 See also: P. Gao, D. Foster, G. Sipos, B. W. Skelton, A. N. Sobolev and R. Dorta, *Organometallics*, 2020, **39**, 556–573.

22 Unpublished results form our group indicate that the R_a,S_a-configured NHC ligands behave somewhat differently, which would be more in line with a rotation around the NHC–[Ir] bond than the windshield-wiper mechanism. For a similar system where the authors believe that a windshield-wiper mechanism is operative, see: E. L. Kolychev, S. Kronig, K. Brandhorst, M. Freytag, P. G. Jones and M. Tamm, *J. Am. Chem. Soc.*, 2013, **135**, 12448–12459.

23 For examples, see: D. H. Woodmansee, A. Pfaltz and P. G. Anderson, *Iridium Catalysis*, Springer-Verlag, Berlin/Heidelberg, 2011, ch. 3, pp. 31–76.

24 The [NTf_2] anion is by now well established in group 11 chemistry/catalysis: (*a*) R. Dorel and A. M. Echavarren, *Chem. Rev.*, 2015, **115**, 9028–9072; (*b*) Z. Zheng, Z. Wang, Y. Wang and L. Zhang, *Chem. Soc. Rev.*, 2016, **45**, 4448–4458; (*c*) W. Zi and F. D. Toste, *Chem. Soc. Rev.*, 2016, **45**, 4567–4589.

25 For an analysis of steric parameters, see: M. S. Sigman and J. J. Miller, *J. Org. Chem.*, 2009, **74**, 7633–7643.

26 (*a*) For an overview, see: *Fluorinated Heterocyclic Compounds: Synthesis, Chemistry, and Applications*, ed. K. L. Kirk and V. A. Petrov, Wiley & Sons, New Jersey, 2009, ch. 3, pp. 91–158; (*b*) For recent synthetic efforts: C. Si, K. R. Fales, A. Torrado, K. Frimpong, T. Kaoudi, H. G. Vandeveer and F. G. Njoroge, *J. Org. Chem.*, 2016, **81**, 4359–4363; (*c*) O. V. Fedorov, M. I. Struchkova and A. D. Dilman, *J. Org. Chem.*, 2017, **82**, 3270–3275.

27 For the synthesis of similar imidazolium fluorides, see: (*a*) B. Ališ and G. Tavčar, *J. Fluorine Chem.*, 2016, **192**, 141–146; (*b*) B. Ališ, M. Tramšek, A. Kokalj and G. Tavčar, *Inorg. Chem.*, 2017, **56**, 10070–10077.

28 Obviously, cationic square-planar complexes are generated during catalysis and would have similar ^{1}H and ^{13}C NMR footprints. Given that our values correspond very closely to values recorded for (R_a,R_a,*S*,*S*)-**2**Cl, involvement of these alternative species can be excluded.

29 A small signal at 192 ppm is also present in the reaction mixture. While we were not able to attribute it, it seems to indicate that a tilted Ir(I) complex is still present. 4-coordinate cationic Ir–NHC complex can be ruled out as species as these shown carbene signals between 200–205 ppm. For details, see: S. V. Gellert, PhD thesis, University of Western Australia, 2017, ch. 3, pp. 117–122.

30 (*a*) N. Z. Menshutkin, *Z. Phys. Chem., Stoechiom. Verwandtschaftsl.*, 1890, **6**, 41–57; (*b*) G. O. Nevstad and J. Songstad, *Acta Chem. Scand.*, 1984, **38b**, 469–477.

31 (*a*) J. Lee, K. J. Stranger, B. C. Noll, C. Gonzalez, M. Marquez and B. D. Smith, *J. Am. Chem. Soc.*, 2005, **127**, 4184–4185; (*b*) B. W. Purse, A. Gissot and J. A. Rebek, *J. Am. Chem. Soc.*, 2005, **127**, 11222–11223.

32 Crystallographically characterized iridium complexes with bound DCM are known, albeit only in the Ir(III) oxidation state, see for example: (*a*) B. Arndtsen and R. G. Bergman, *Science*, 1995, **270**, 1970–1973; (*b*) E. Piras, F. Läng, H. Rüegger, D. Stein, M. Wörle and H. Grützmacher, *Chem.–Eur. J.*, 2006, **12**, 5849–5858; (*c*) S. Gruber, M. Neuburger and A. Pfaltz, *Organometallics*, 2013, **32**, 4702–4711; (*d*) A. R. Chianese, M. J. Drance, K. H. Jensen, S. P. McCollom, N. Yusufova, S. E. Shaner, D. Y. Shopov and J. A. Tendler, *J. Am. Chem. Soc.*, 2014, **33**, 457–464.

33 (*a*) J. H. Cho and B. M. Kim, *Org. Lett.*, 2003, **5**, 531–533; (*b*) D. W. Knight, I. R. Morgan and A. J. Proctor, *Tetrahedron Lett.*, 2010, **51**, 638–640.

34 (*a*) A. Ogawa and D. Curran, *J. Org. Chem.*, 1997, **62**, 450–451; (*b*) P. Tolstoy, M. Engman, A. Paptchikhine, J. Bergquist, T. L. Church, A. W. M. Leung and P. G. Andersson, *J. Am. Chem. Soc.*, 2009, **131**, 8855–8860; (*c*) W. J. Yoo and S. Kobayashi, *Green Chem.*, 2014, **16**, 2438–2442; (*d*) J. Liu, S. Krajangsri, T. Singh, G. De Seriis, N. Chumnanvej, H. Wu and P. G. Andersson, *J. Am. Chem. Soc.*, 2017, **139**, 14470–14475.

35 (*a*) S. Adachi, K. Koike and I. Takayanagi, *Pharmacology*, 1996, **53**, 250–258; (*b*) J.-C. Carry, V. Cetral, F. Halley, K. A. Karlsson, L. Schio and F. Thompson, Patent Appl. WO 2011001114, 2011; (*c*) V. Certal, F. Halley, A. Virone-Oddos, C. Delorme, A. Karlsson, A. Rak, F. Thompson, B. Filoche-Romme, Y. El-Ahmad, J. C. Carry, P. Y. Abecassis, P. Leujeune, L. Vincent, H. Bonnevaux, J. P. Nicolas, T. Bertrand, J. P. Marquette, N. Michot, T. Benard, P. Below, I. Vade, F. Chatreaux, G. Lebourg, F. Pilorge, O. Angouillant-Boniface, A. Louboutin, C. Lengauer and L. Schio, *J. Med. Chem.*, 2012, **55**, 4788–4805; (*d*) V. Certal, J. C. Carry, F. Halley, A. Virone-Oddos, F. Thompson, B. Filoche-Romme, Y. El-Ahmad, A. Karlsson, V. Charrier, C. Delorme, A. Rak, P. Y. Abecassis, C. Amara, L. Vincent, H. Bonnevaux, J. P. Nicolas, M. Mathieu, T. Bertrand, J.-P. Marquette, N. Michot, T. Benard, M.-A. Perrin, O. Lemaitre, S. Guerif, S. Perron, S. Monget, F. Gruss-Leleu, G. Doerflinger, H. Guizani, M. Brollo, L. Delbarre, L. Bertin, P. Richepin, V. Loyau, C. Garcia- Echeverria, C. Lengauer and L. Schio, *J. Med. Chem.*, 2014, **57**, 903–920; (*e*) P. L. Bedard, M. A. Davies, S. Kopetz, D. Juric, G. I. Shapiro, J. J. Luke, A. Spreafico, B. Wu, C. Castell, C. Gomez, S. Cartot-Cotton, F. Mazuir, M. Dubar, S. Micallef, B. Demers and K. T. Flaherty, *Cancer*, 2018, **124**, 315–324.

36 For two representative recent examples: (*a*) T. Touge and T. Arai, *J. Am. Chem. Soc.*, 2016, **138**, 11299–11305; (*b*) Z. Yang, F. Chen, Y. He, N. Yang and Q.-H. Fan, *Angew. Chem., Int. Ed.*, 2016, **55**, 13863–13866.

37 For select references: (*a*) F. O. Arp and G. C. Fu, *J. Am. Chem. Soc.*, 2006, **128**, 14264–14265; (*b*) K. Saito, Y. Shibata, M. Yamanaka and T. Akiyama, *J. Am. Chem. Soc.*, 2013, **135**, 11740–11743; (*c*) J. I. Murray, N. J. Floden, A. Bauer, N. D. Fessner, D. L. Dunklemann, O. Bob-Egbe, H. S. Rzepa, T. Buergi, J. Richardson and A. C. Spivey, *Angew. Chem., Int. Ed.*, 2017, **56**, 5760–5764.

38 E. Ascic and S. Buchwald, *J. Am. Chem. Soc.*, 2015, **137**, 4666–4669.

39 A. L. Casalnuovo, J. C. Calabrese and D. Milstein, *J. Am. Chem. Soc.*, 1988, **110**, 6738–6744.

40 S. C. Ensign, E. P. Vanable, G. D. Kortman, L. J. Weir and K. L. Hull, *J. Am. Chem. Soc.*, 2015, **137**, 13748–13751.

41 Y. Kashiwame, S. Kuwata and T. Ikariya, *Organometallics*, 2012, **31**, 8444–8455.

42 A. Otero, A. Lara-Sánchez, J. A. Castro-Osma, I. Márquez-Segovia, C. Alonso-Moreno, J. Fernández-Barza, L. F. Sánchez-Barba and A. M. Rodríguez, *New J. Chem.*, 2015, **39**, 7672–7681.

43 A. C. Sykes, P. White and M. Brookhart, *Organometallics*, 2006, **25**, 1664–1675.

44 (*a*) *Modern Physical Organic Chemistry*, ed. E. Anslyn, 2006, pp. 422–428; (*b*) *Isotope Effects*, ed. M. Wolfsberg, W. A. Van Hook and P. Paneth, 2009, ch. 10, pp. 313–342.